Monthly Notices
of the
ROYAL ASTRONOMICAL SOCIETY

MNRAS **490,** 5798–5806 (2019) doi:10.1093/mnras/stz2967

Radio spectral properties of cores and extended regions in blazars in the MHz regime

D. d'Antonio,[1]★ M. Giroletti,[2] G. Giovannini[1,2] and A. Maini[1,2,3]

[1]*Dipartimento di Fisica e Astronomia, Università di Bologna, via Gobetti 93/2, 40129 Bologna, Italy*
[2]*INAF – IRA, via Gobetti 101, 40129 Bologna, Italy*
[3]*Department of Physics and Astronomy, Macquarie University, Balaclava Road, North Ryde, NSW, 2109, Australia*

Accepted 2019 October 14. Received 2019 October 13; in original form 2019 April 26

ABSTRACT

Low-frequency radio surveys allow in-depth studies and new analyses of classes of sources that were previously known and characterized only in other bands. In recent years, low radio frequency observations of blazars have become available as a result of new surveys, such as the GaLactic and Extragalactic All-sky Murchison Widefield Array (MWA) survey (GLEAM). We search for gamma-ray blazars in a low-frequency ($\nu < 240$ MHz) survey, to characterize the spectral properties of the spatial components. We cross-correlate GLEAM with the fourth catalogue of active galactic nuclei (4LAC) detected by the *Fermi* satellite. This improves on previous works by using a low-frequency catalogue that is wider and deeper, with a better spectral coverage and the latest and most sensitive gamma-ray source list. Compared with a previous study based on the commissioning survey, the detection rate increased from 35 to 70 per cent. We include data from the Australia Telescope 20-GHz (AT20G) survey in order to extract high-frequency high-angular resolution information about the radio cores of blazars. We find low radio frequency counterparts for 1274 out of 1827 blazars in the range of 72–231 MHz. Blazars have flat spectra at the ∼100-MHz regime, with a mean spectral index $\alpha = -0.44 \pm 0.01$ (assuming $S_\nu \propto \nu^\alpha$). Low synchrotron peaked objects have a flatter spectrum than high synchrotron peaked objects. Low frequency radio and gamma-ray emissions show a significant but scattered correlation. The ratio between lobe and core radio emission in gamma-ray blazars is smaller than previously estimated.

Key words: astronomical data bases: miscellaneous – catalogues – galaxies: jets – galaxies: nuclei – quasars: general.

1 INTRODUCTION

Blazars are the most extreme objects in the class of active galactic nuclei (AGNs). In these objects, the relativistic plasma jets produced by the central supermassive black hole are closely aligned with the line of sight, which results in an emission amplified by the Doppler boosting effect. For this reason, these objects are detected at cosmological distances. Their emission is mainly non-thermal, with a spectral energy distribution (SED) characterized by two humps (Blandford & Rees 1978; Abdo et al. 2010c; Urry & Padovani 1995).

Blazars are composed of two main classes: BL Lac objects (BL Lacs) with weak emission lines in optical spectra, and flat-spectrum radio quasars (FSRQs) with strong emission lines in the optical band (Stickel et al. 1991). Furthermore, blazars can be classified based on the position of the synchrotron peak frequency. Low synchrotron peaked (LSP) sources have peak frequency smaller than $\nu_{\rm peak} < 10^{14}$ Hz; intermediate synchrotron peaked (ISP) sources have peak frequency in the range $10^{14} < \nu_{\rm peak} < 10^{15}$ Hz; and high synchrotron peaked (HSP) sources have peak frequency greater than $\nu_{\rm peak} > 10^{15}$ Hz (Ackermann et al. 2015).

In this paper, we present the results of an investigation of the spectral properties of gamma-ray blazars carried out using a new, wide-area, high-sensitivity, large-bandwidth sky survey at low radio frequencies: the GaLactic and Extragalactic All-sky Murchison Widefield Array (MWA) Survey (GLEAM; Hurley-Walker et al. 2017), produced by the MWA (Tingay et al. 2013). GLEAM covers about 24 831 deg^2 in the southern sky with a bandwidth between 72 and 231 MHz, and contains 307 455 objects. The advantage of GLEAM is that it allows us to perform, for the first time, an accurate study of blazars at low radio frequency in the MHz regime.

Moreover, because of the Large Area Telescope (LAT) on board the *Fermi* satellite, in the last few years the astrophysics of

★ E-mail: daniele.dantonio364@gmail.com

gamma-rays has greatly improved. We cross-correlate the GLEAM catalogue with the fourth catalogue of AGNs detected by the *Fermi* satellite (4LAC; *Fermi*-LAT collaboration 2019b), to study the connection between the radio band and the gamma band. The 4LAC catalogue is a subsample of gamma-ray blazars, extracted by the LAT collaboration from the fourth *Fermi*-LAT catalogue of gamma-ray sources (4FGL; *Fermi*-LAT collaboration 2019a), which is the latest and deepest source list in the energy range from 50 MeV to 1 TeV.

In recent years, several studies carried out at low frequency (i.e. below ∼1GHz) have allowed us to obtain more information about blazars. The discovery that blazars have flat radio spectra in the regime of hundreds of MHz is particularly intriguing. Indeed, flat radio spectra are expected at the GHz regime (Ivezić et al. 2002; Healey et al. 2007; Kimball & Ivezić 2008), but recently it has become evident that this flat spectral behaviour is still present at lower frequencies. Massaro et al. (2013a, 2014) have found gamma-ray blazars with radio counterparts that show flat spectra in the interval between ∼325 MHz and 1.4 GHz. This result was confirmed by Nori et al. (2014) in a slightly less wide frequency range (352–1400 MHz). Massaro et al. (2013b) performed a study in a wider frequency interval (74–1400 MHz and 1.4–4.85 GHz), for which 60 per cent of gamma-ray blazars have flat spectra and 99 per cent of the whole sample present radio spectra evidently influenced by a flat core component. This work suggests that blazar spectra are characterized by a beaming effect due to particles accelerated in relativistic jets even down to 74 MHz. Furthermore, Giroletti et al. (2016, hereafter G16) Fan & Wu (2018) and Mooney et al. (2019) highlighted a gamma/radio correlation which, however, becomes weaker at lower radio frequency. All these studies show that the flat core component has an important contribution at low radio frequencies (from 74 to 1400 MHz).

In previous work, G16 cross-correlated the 3LAC catalogue with the MWA Commissioning Survey (MWACS) of compact low-frequency sources (Hurley-Walker et al. 2014), a preliminary survey carried out using the MWA. Given the wider sky area, the deeper sensitivity and the better spectral coverage of GLEAM with respect to MWACS, we decided to significantly improve the constraints derived in the previous work about the low-frequency properties (hundreds of MHz) of gamma-ray blazars. We find 1274 out of 1827 gamma-ray blazars. This number of sources with a radio counterpart that we analysed is larger than in another work based on the Low Frequency Array (LOFAR; Mooney et al. 2019) by a factor of 13. The number of objects in our sample is also larger than in the Giant Metrewave Radio Telescope (GMRT; Fan & Wu 2018) data by a factor of 1.3. In detail, Mooney et al. (2019) have a total of 102 sources and find a radio counterpart for all 98 objects from the Third *Fermi*-LAT Source Catalogue (3FGL; Acero et al. 2015), whereas Fan & Wu (2018) find 983 out of 1328 sources from the Tata Institute of Fundamental Research GMRT Sky Survey (TGSS; Intema et al. 2017). Moreover, we use the Australia Telescope 20-GHz survey (AT20G; Murphy et al. 2010) to characterize the nuclear emission, when possible.

In Section 2, we describe all the catalogues, including properties such as their frequency range, sky area, number of sources and the counts and types of objects for every survey. In Section 3, we explain the selection criteria of the samples we utilized (gamma-ray blazars in the GLEAM and AT20G surveys). The results concerning the spectral properties are presented in Section 4, while in Section 5 we discuss the results and give our conclusions.

In this paper, we adopt a ΛCDM cosmology with $h = 0.71$, $\Omega_{\rm m} = 0.27$ and $\Omega_{\Lambda} = 0.73$ (Komatsu et al. 2009). Also, the radio spectral index α is defined by the flux density S_ν and the frequency ν adopting the convection $S_\nu \propto \nu^{\alpha}$, while the gamma-ray photon index Γ respects the relation $\mathrm{d}N_{\rm photon}/\mathrm{d}E \propto E^{-\Gamma}$, where it is defined by the photon flux $\mathrm{d}N$ (i.e. the number of photons per square centimetre per second) and the energy E (note that G16 used $S_\nu \propto \nu^{-\alpha}$ and $\mathrm{d}N_{\rm photon}/\mathrm{d}E \propto E^{-\Gamma}$).

2 CATALOGUES

2.1 GLEAM catalogue

GLEAM observations began in 2013 August. The first two runs of observations (concluded in 2014 July and 2015 July, respectively) were carried out in the frequency range ∼72–231 MHz. A third run of observations, concluded in 2016 July, was performed at higher radio frequencies (∼250–310 MHz), but these observations are not part of this work as we were interested in analysing the lowest frequency range. The GLEAM survey covers the entire south sky up to +30° of celestial declination, excluding the Galactic latitudes within 10° from the Galactic plane and the Magellanic Clouds (Hurley-Walker et al. 2017). This is also the sky area where GLEAM overlaps the AT20G. The final catalogue is mainly composed of extragalactic sources.

GLEAM has a resolution down to ∼2 arcmin, and in total contains 307 455 radio sources. For every source, both peak and integrated flux density centred at 200 MHz are reported, as well as 20 separate flux density measurements across the 72–231 MHz range, each based on a bandwidth 7.68 MHz wide. The survey is reported to be 90 per cent complete at 170 mJy, and 50 per cent complete at 55 mJy (see Hurley-Walker et al. 2017 for more details).

2.2 AT20G catalogue

The AT20G is a radio survey performed in the period between 2004 and 2008, at 20 GHz with the Australia Telescope Compact Array (ATCA). It covers the whole sky south of 0° declination. Therefore, the AT20G covers the whole south sky area covered by GLEAM. It is the largest and most sensitive survey of the sky ever carried out at this frequency, with a flux density limit above 40 mJy.

The final catalogue is composed of 5890 objects, and all the sources have a flux density greater than 50 mJy at 20 GHz. Moreover, some sources are also provided with 5 and 8 GHz flux densities. This catalogue has been fundamental for the study of radio emission in flat-spectrum sources, such as the cores of radio-loud AGNs (Mahony et al. 2010). We used the data from version 1.0 in Vizier.

2.3 4FGL catalogue

The 4FGL (Fermi-LAT collaboration 2019a) is a catalogue of gamma-ray sources observed by *Fermi* over the first 8 yr of the mission, based on data in the energy range from 50 MeV to 1 TeV. With twice as much exposure as well as a number of analysis improvements, including an updated model for the Galactic diffuse gamma-ray emission, it supersedes the third *Fermi*-LAT catalogue (3FGL) and the earlier releases: the LAT Bright Source List (0FGL; Abdo et al. 2009), the First *Fermi*-LAT (1FGL; Abdo et al. 2010b) and the Second *Fermi*-LAT (2FGL; Nolan et al. 2012) catalogues. Moreover, including an update model for the Galactic diffuse gamma-ray emission, the 4FGL catalogue also supersedes

its early release (FLY8[1]) which was released by the *Fermi*-LAT Collaboration. The 4FGL catalogue is deeper than the previous catalogues in the 0.1–300 GeV energy range.

The total number of sources in the 4FGL is 5065 above 4σ, for each of which are reported position, significance, photon index and gamma-ray flux. The catalogue also lists the flux in various energy ranges, as well as the total flux in yearly and bi-monthly time intervals constituting the 8 yr of observations. The distribution of the 95 per cent confidence error radius (geometric mean of semimajor and semiminor axes of the 95 per cent confidence error ellipse) of the sample has the highest peak at ∼4 arcmin. This is verified for all sources at high Galactic latitudes ($|b| > 10^{\circ}$). Most sources are associated with blazars, while a significant number (∼ 26 per cent) do not have a counterpart at low frequencies. We accessed the complete catalogue on the *Fermi* Science Support Center web site.[2] The *Fermi*-LAT collaboration released the data.

2.4 4LAC catalogue: a subset of the 4FGL

The 4LAC is a subset of the 4FGL catalogue that includes all gamma-ray sources at high Galactic latitudes ($|b| > 10^{\circ}$) associated with AGNs, either as a result of a Bayesian association (Abdo et al. 2010a) or based on the likelihood ratio technique (Ackermann et al. 2011b). At the time of writing, the publicly available version of the 4LAC[3] (released by the *Fermi*-LAT team) includes 2863 blazars. We further restrict this list to the 2682 objects for which we were able to recover the radio flux density from the NRAO VLA Sky Survey (NVSS) or the Sydney University Molonglo Sky Survey (SUMSS).

Because the 4LAC is a gamma-ray catalogue, the most abundant type of source is blazars (98 per cent of the total sources, both as confirmed and candidates). The catalogue also contains information about the low frequency counterparts (as the VLBI identifier and position, and the *Gaia* identifier), the redshift and the position of the peak of the synchrotron component of the SED. According to the SED classification, the subset is composed of 1125 LSPs, 399 ISPs and 362 HSPs. According to the spectroscopic classification, the subset is composed of 644 FSRQs, 1036 BL Lacs and 939 blazar candidates of unknown/uncertain type (BCU). This last category includes both confirmed blazars of uncertain type – those included in the BZCat catalogue (Massaro et al. 2015) and provided with the optical spectrum – and blazar candidates lacking a proper optical spectroscopic analysis but characterized by the typical properties of blazars (e.g. two humped SED or flat radio spectra). However, several optical spectroscopic investigations (e.g. Álvarez Crespo et al. 2016; Massaro et al. 2016; Paiano et al. 2017a, 2017b; Peña-Herazo et al. 2017; Marchesi, Kaur & Ajello 2018) have demonstrated that most BCUs are evidently BL Lacs.

3 CROSS-CORRELATION OF THE CATALOGUES

The cross-matching of the catalogues was performed using TOPCAT (Taylor 2005). In this section, we provide some details on the procedure that we applied.

[1] https://fermi.gsfc.nasa.gov/ssc/data/access/lat/fl8y/
[2] https://fermi.gsfc.nasa.gov/ssc/data/access/
[3] ftp://www.cenbg.in2p3.fr/astropart/Fermi/4LAC/

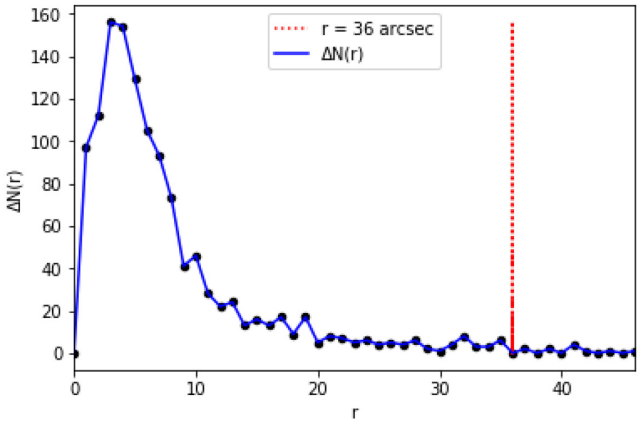

Figure 1. Difference $\Delta N(r)$ between the number of cross-matches $N(r)$ at a given radius r and the same quantity at $r - \Delta r$ between 0 and 46 arcsec. Note also that $\Delta r = 1$ arcsec. The vertical red dotted line highlights the matching radius at 36 arcsec, which is the value we have adopted to create the sample 4LAC–GLEAM.

3.1 Cross-match of 4LAC–GLEAM

Initially, we followed the same procedure that we had adopted for the 3LAC–MWACS cross-match in G16. For the blazar positions, we assumed a 5-arcsec error radius, because the radio counterparts of LAT blazars generally come from interferometric surveys in the GHz domain, such as AT20G, NVSS (Condon et al. 1998), SUMSS (Mauch et al. 2003), Faint Images of the Radio Sky at Twenty-centimeters (FIRST; Helfand, White & Becker 2015) and the Australia Telescope PMN follow-up survey (PMN; McConnell et al. 2012); often, they even have submilliarcsecond accuracy as provided by VLBI observations. For the GLEAM sources, we considered the 95 per cent error ellipse obtained as 1.621 × the uncertainties reported on the RA and Dec. coordinates. This resulted in a total of 1012 matches, which was already a significant increase over the 3LAC–MWACS results, in terms of both the sheer number of sources (multipied by a factor of 5.4) and the detection rate (with a 15 per cent increase). To assess the number of spurious matches, we created 100 fake gamma-ray catalogues by shifting the position of the blazars by 2° in random directions, and we cross-correlated these random lists with GLEAM. Most of these cross-comparisons resulted in no matches, or very few matches (1.55 on average), so that the fraction of spurious matches in our list turns out to be very small (0.0015). As this fraction remains small, even increasing the matching radii, while the number of real matches keeps increasing, we concluded that the use of the nominal positional uncertainties was actually leading us to underestimate the number of real matches. One possible reason is that the centroid of the MHz and GHz emission regions are offset from each other by more than their respective positional uncertainties. We might expect a weak contribution from the extended region. Consequently, even a slight misalignment of the jet axis (e.g. 10°), for a 100 kpc lobe at $z = 0.05$ can result in a projected displacement of ∼17 arcsec from the core, and can thus result in a missing match.

Therefore, we adopted the procedure developed by Massaro et al. (2013a, 2013b), and determined a matching radius of 36 arcsec, above which the number of matches obtained using the simulated gamma-ray catalogues exceeds that of the real catalogue. Following the same approach used by Massaro et al. (2013b), Fig. 1 highlights the difference between the number of cross-matches $N(r)$ at a given

radius r and the same quantity at $r - \Delta r$, that is, $\Delta N(r) = N(r) - N(r - \Delta r)$, where $\Delta r = 1$ arcsec.

Our cross-matching provided us with 1274 objects, all unique. Using the same technique described above (simulating 100 gamma-ray catalogues, each obtained by shifting every original gamma-ray blazar by 2° in a random direction), we estimate the fraction of spurious associations in our final list to be ∼0.0055.

According to the SED classification, the matched sources are 716 LSPs, 130 ISPs and 115 HSPs, while according to the spectroscopic classification these matched sources are 406 FSRQs, 384 BL Lacs and 456 BCUs. The value of 1274 matches corresponds to a high detection rate of ∼ 70 per cent, implying that most blazars are detected at low radio frequency with GLEAM sensitivity. To check that all matches are unique, we searched for the GLEAM counterparts of the 4LAC sources, and vice versa, and we verified that the two cross-matching catalogues contained the same sources.

3.2 Cross-match of 4LAC–AT20G

From the cross-match between the 4LAC (2682 objects) and the AT20G (5890 objects), we obtained a sample composed of 677 gamma-ray blazars detected at high radio frequency. We determined a matching radius of 7 arcsec by using the same method adopted to create the sample 4LAC–GLEAM (see Section 3.1). Even in this case, values above the matching radius chosen exceed the number of real matches.

3.3 Cross-match of 4LAC–GLEAM versus 4LAC–AT20G

Eventually, we cross-matched the sample of 1274 blazars detected at low radio frequency (see Section 3.1), with the sample of 677 blazars detected at high radio frequency (see Section 3.2). This cross-match was realized based on the coincidence of the 4LAC counterpart, so it did not require any positional matching (i.e. we assumed that whenever a gamma-ray blazar has both a GLEAM and an AT20G counterpart, the two are associated with each other). This final catalogue is composed of 612 objects.

4 RESULTS

In this section, we report the results on the detection rates and the spectral properties of the gamma-ray blazars detected with GLEAM at low radio frequencies, and considerations about emission from the core and the extended region of AGNs.

4.1 Detection rate: a step forward from 3LAC–MWACS to 4LAC–GLEAM

Table 1 gives the values of the detection rates for gamma-ray blazars, in the MWACS and GLEAM catalogues. Data for the MWACS and 3LAC catalogues are reported in G16. We summarize these results as follows.

(i) Analysing the detection rate of sources classified following the SED, the largest group of detected sources is that of the LSPs, followed by the ISPs and the HSPs. This is not surprising, as the LSPs are the biggest group of sources in the starting sample (4LAC), and their detection rate was already the greatest in the 3LAC–MWACS cross-match.

(ii) Analysing the detection rate of sources classified following the spectroscopic classification, we notice that the largest detection rate for the FSRQs, while BL Lacs and BCUs have similar detection rates. This confirms the optical spectroscopic campaigns carried out in recent years and already mentioned in Section 2.3.1 (Álvarez Crespo et al. 2016; Massaro et al. 2016; Paiano et al. 2017a, 2017b; Peña-Herazo et al. 2017; Marchesi et al. 2018).

(iii) The detection rate increased to 70 per cent for 4LAC–GLEAM compared with 35 per cent for 3LAC–MWACS. In comparison with the previous study based on the commissioning survey (G16), these constitute 14.6× and 2× increases in the total number of sources and in the detection rate, respectively. It is worth noting that the detection rate grows for every type of object, considering both the SED and spectroscopic classification. Nearly all FSRQs (92 per cent) are now detected. The improvement in the detection rate is especially impressive for the faintest classes such as the BL Lacs (from 22 per cent in 3LAC–MWACS to 58 per cent in 4LAC–GLEAM) and the BCUs (from 18 per cent in 3LAC–MWACS to 66 per cent in 4LAC–GLEAM).

Table 1. Detection rates for 4LAC sources, in the MWACS and GLEAM catalogues.

Class	3LAC–MWACS		4LAC–GLEAM	
	Ratio	Det. rate	Ratio	Det. rate
Total	87 / 247	35%	1274 / 1827	70%
FSRQ	52 / 71	73%	406 / 440	92%
BCU	16 / 89	18%	456 / 689	66%
BLL	19 / 87	22%	384 / 659	58%
LSP	67 / 128	52%	716 / 825	87%
ISP	11 / 37	30%	130 / 255	51%
HSP	9 / 68	13%	115 / 248	46%

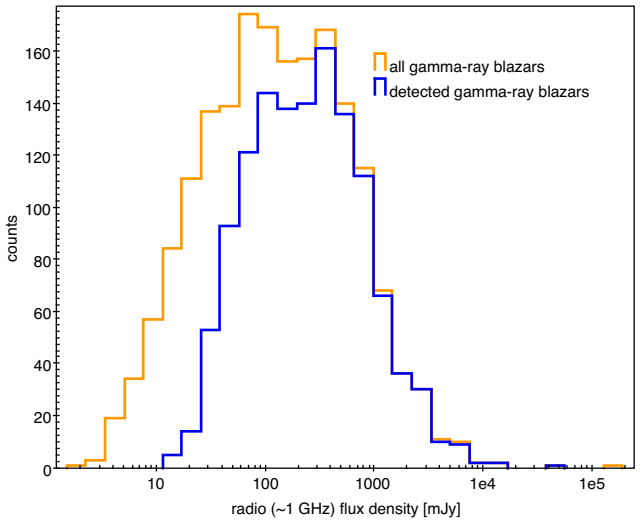

Figure 2. Distribution of the 1-GHz flux densities for the entire 4LAC sample in the GLEAM sky (orange) and for the 4LAC sources with a GLEAM counterpart (blue). Notice the gamma-ray blazars with flux density larger than the GLEAM sensitivity (6–10 mJy beam^{-1}) that were undetected in our cross-matching. These sources must have an inverted spectrum.

4.2 Detection rate as a function of radio and gamma emission

Figs 2 and 3 show the detection rate as a function of the flux density at the GHz regime and of the gamma-ray energy flux at $E >$ 100 MeV, respectively. In fact, in these histograms, we compare the 4LAC sample with the GLEAM sample. We describe the relative results, as follows.

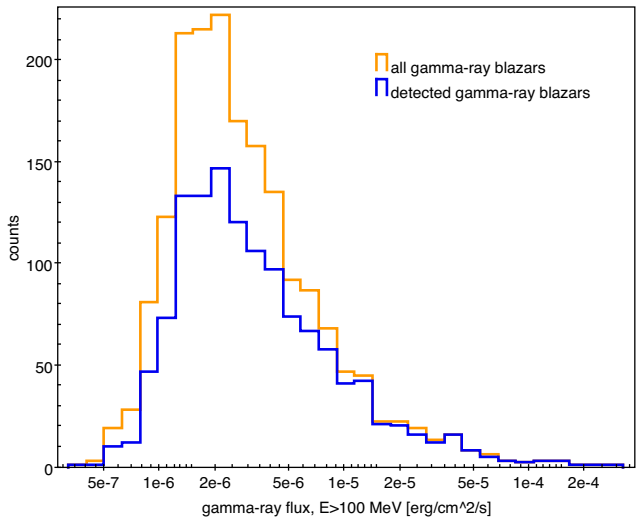

Figure 3. Distribution of the gamma-ray flux (at $E > 100$ MeV) for the entire 4LAC sample in the GLEAM sky (orange) and for the 4LAC sources with GLEAM counterpart (blue).

(i) The detection rate grows with the brightness of the objects, in both the radio and gamma-ray band. This behaviour was quite predictable. The gamma-ray source in Fig. 2 with a powerful radio flux density ($S_{1\,\mathrm{GHz}} \sim 10^5$ mJy) that is not detected in GLEAM is the famous radio galaxy Centaurus A, lying at very low redshift ($z = 0.004$) and with bright radio lobes. This source is not included in the GLEAM catalogue because of its bright side lobes. As radio galaxies constitute a tiny fraction of the 4LAC, which we are not considering in this work, this missing match is not a concern.

(ii) In Fig. 3, the distribution of the gamma-ray flux densities has the typical shape of the complete source-count distributions: the number of detected sources increases regularly as the flux density decreases, until a sudden turnover is reached at the instrument sensitivity limit. In the same way, the brightest gamma-ray sources almost always have a GLEAM counterpart, and the GLEAM detection rate decreases only for fainter sources.

(iii) In Fig. 2, the distribution of the radio flux densities is far less symmetric, and lacks any well-defined turnover at low flux densities.

(iv) In Fig. 2, an interesting feature is the large number of gamma-ray blazars with GHz radio flux density larger than the GLEAM sensitivity (6–10 mJy beam^{-1}), which actually was undetected in our cross-matching. These sources must have an inverted spectrum.

4.3 Spectral index

The population of gamma-ray blazars detected at low radio frequencies (i.e. in the 72–231 MHz range), presents a radio spectrum that is flatter than the rest of the GLEAM population. This result is shown in Fig. 4, which plots the normalized and the cumulative distributions of the GLEAM blazars' spectral indices, both for the whole survey and for the subset of detected sources. In Table 2, we report the mean spectral indices for different frequency ranges (76–115, 115–151, 151–189 and 189–227 MHz). Even this table shows that gamma-ray blazars spectra are flatter than all the rest of the GLEAM sources.

In Table 3, we report the mean values of the spectral index, for the whole population of the detected blazars, and for the subclasses obtained based on SED classification and on spectroscopic classification. Notice that the GLEAM catalogue does not report a spectral index for all sources, as some objects have a complex spectrum that is difficult to fit with a single power law. Therefore, for each class, we report both the total number of objects and the number of objects actually provided with a value of the spectral index.

From Table 3, it is possible to see that the spectral indices characteristic of LSPs and HSPs are significantly different $\Delta\alpha = \alpha_{\mathrm{LSP}} - \alpha_{\mathrm{HSP}} = 0.19 \pm 0.04$. To understand if this gap is an intrinsic difference between the two classes, we first had to remove the possible dependence on the different redshift distributions for the two types (with LSP blazars being typically at higher z than HSPs). Therefore, we considered the rest-frame spectral indices, taking advantage of the wide spectral coverage that characterizes the GLEAM survey, as well as of its spectral resolution that provides 20 separate flux density measurements in the 72–231 MHz range (see Section 2.1). We allocated our blazars into six redshift bins according to their redshift, each $\Delta z = 0.2$ wide and centred on $z = 0.2$, 0.4, 0.6, 0.8, 1.0 and 1.2, respectively. To compute the individual spectral indices, we then assumed the formula $\alpha = \log(S_1/S_2)/\log(\nu_1/\nu_2)$ where we used the integrated radio flux densities measured by GLEAM in different frequency bands, according to the redshift bin.

In detail, for sources in the bin centred at $z = 0.2$, we computed the spectral index based on the radio flux densities measured in the bands centred at 174 and 189 MHz (i.e. $S_{174\,\mathrm{MHz}}$ and $S_{189\,\mathrm{MHz}}$); similarly, for sources in the bins centred on $z = 0.4$, 0.6, 0.8, 1.0 and 1.2, we used the following pairs: $S_{151\,\mathrm{MHz}} - S_{166\,\mathrm{MHz}}$, $S_{130\,\mathrm{MHz}} - S_{143\,\mathrm{MHz}}$, $S_{115\,\mathrm{MHz}} - S_{130\,\mathrm{MHz}}$, $S_{107\,\mathrm{MHz}} - S_{115\,\mathrm{MHz}}$ and $S_{99\,\mathrm{MHz}} - S_{107\,\mathrm{MHz}}$, respectively.

The reason for this procedure is that when rest-framed for the corresponding redshift – that is, $\nu_{\mathrm{rest\text{-}frame}} = \nu_{\mathrm{obs}}(1+z)$ – these bands of observation all refer to similar intervals of emission frequency, in the range between ∼215 and ∼230 MHz. This guarantees that all the computed spectral indices refer to the same spectral region. We are therefore sure that we are comparing consistent areas of the radio spectrum. Table 4 displays both the bands of observations and the corresponding emitted range frequency with the corresponding bin of redshift.

Finally, Table 5 shows the average values of intrinsic spectral indices for the different classes calculated using the rest-frame values in single sub-bands. The total number of objects in each class has decreased, because we had to discard sources without a reliable spectral index in the relevant sub-band. Moreover, intrinsic scatter of spectral indices becomes larger when they are measured in single sub-bands as a result of the poorer signal-to-noise when using narrower frequency intervals. As we are narrowing the spectral index to the highest frequency band, all values tend to become flatter. In any case, the differences between different types are no longer significant, not simply because of the larger standard deviation but also considering the mean value.

4.4 Gamma–radio correlation

The distribution in Fig. 5 shows that gamma-ray blazars are brighter in radio, and that they are almost always detected in GLEAM (see Fig. 2). This finding suggests a very interesting possible correlation between radio and gamma-ray emissions. To test this possibility, we checked whether the correlation holds even considering the types of blazars as classified according to their spectra and their SEDs.

In the top row of Fig. 6, we show scatter plots of the gamma-ray fluxes as a function of radio flux densities at both 200 MHz (from GLEAM; left panel) and at ∼1 GHz (from 4LAC; right panel), with

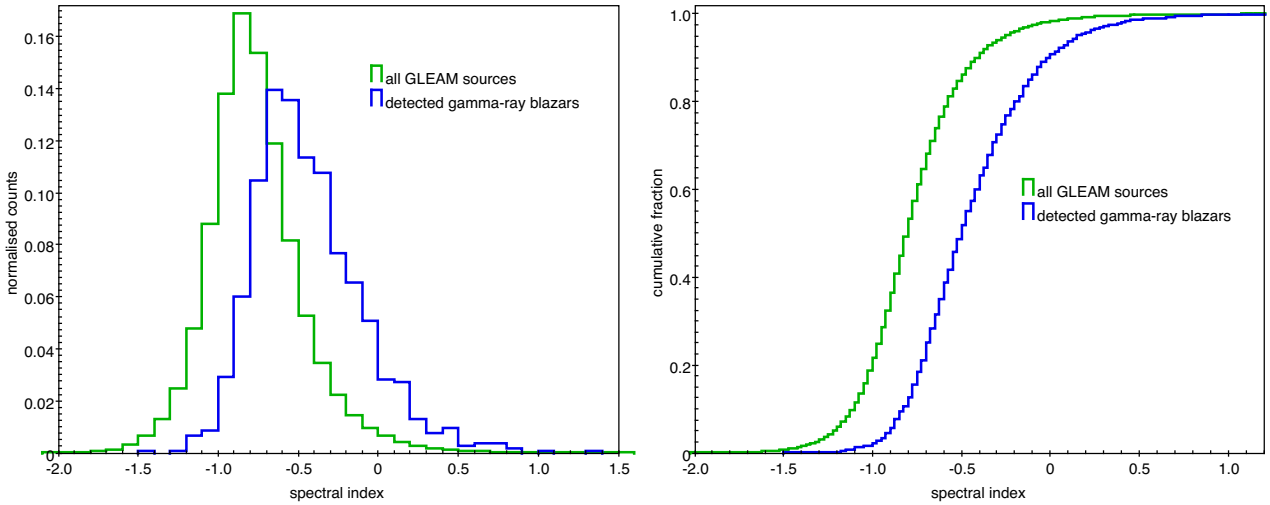

Figure 4. Probability density (left) and cumulative distribution (right) functions of the spectral indices (α), both for the blazars detected at low frequencies (blue) and for all the GLEAM sources (green).

Table 2. Mean values of the spectral indices in the frequency ranges 76–115, 115–151, 151–189 and 189–227 MHz, for the whole GLEAM population and for the population of detected blazars. For each frequency interval, we also report the total number of sources for which it is possible to estimate the spectral indices. The errors have been computed as standard deviations of the mean.

Population	Sources	76–115 MHz		115–151 MHz		151–189 MHz		189–227 MHz	
		Sources	$\langle\alpha\rangle \pm \sigma_{\langle\alpha\rangle}$	Sources	$\langle\alpha\rangle \pm \sigma_{\langle\alpha\rangle}$	Sources	$\langle\alpha\rangle \pm \sigma_{\langle\alpha\rangle}$	Sources	$\langle\alpha\rangle \pm \sigma_{\langle\alpha\rangle}$
GLEAM	307 455	281 817	-0.62 ± 0.03	299 743	-0.63 ± 0.04	304 161	-0.52 ± 0.04	304 637	-0.67 ± 0.05
Blazars	1274	1188	-0.38 ± 0.04	1252	-0.36 ± 0.04	1266	-0.29 ± 0.04	1267	-0.36 ± 0.05

Table 3. Mean values of the spectral index for the whole population of the detected blazars, and for the subclasses obtained based on SED classification and on spectroscopic classification. We report both the total number of blazars detected at low frequencies in GLEAM, and the number of objects for which GLEAM provides a values for the spectral index α. The associated errors have been computed as standard deviations of the mean.

Class	Total sources	Sources with spectral index	$\langle\alpha_{\rm GLEAM}\rangle \pm \sigma_{\langle\alpha_{\rm GLEAM}\rangle}$
Total	1274	1067	-0.44 ± 0.01
FSRQ	406	372	-0.36 ± 0.02
BCU	456	367	-0.50 ± 0.02
BLL	384	302	-0.44 ± 0.02
LSP	716	637	-0.37 ± 0.01
ISP	130	94	-0.49 ± 0.03
HSP	115	85	-0.56 ± 0.03

Table 4. Observed and emitted frequency ranges for every bin of redshift.

Central redshift in bin	Observed frequencies (MHz)	Emitted frequencies (MHz)
1.2	99–107	218–235
1.0	107–115	214–230
0.8	115–130	207–234
0.6	130–143	208–229
0.4	151–166	211–232
0.2	174–189	209–227

Table 5. Mean values of the intrinsic spectral index, and for the subclasses obtained based on SED classification and on spectroscopic classification. We report the number of objects for which we have been able to provide the values for the rest-frame spectral index $\alpha_{\rm rf}$. The associated errors have been computed as standard deviations of the mean.

Class	Sources at rest frame	$\langle\alpha_{\rm rf}\rangle \pm \sigma_{\alpha_{\rm rf}}$
Total	1277	-0.32 ± 0.03
FSRQ	523	-0.29 ± 0.04
BCU	348	-0.38 ± 0.06
BLL	372	-0.29 ± 0.06
LSP	789	-0.31 ± 0.04
ISP	115	-0.21 ± 0.11
HSP	101	-0.31 ± 0.10

the detected blazars classified according to their optical spectra. In the bottom panels, the same quantities are plotted, but the blazars are classified according to their SED type. The data are distributed with a large scatter; dashed lines report the best-fitting trend, whose significance needs to be assessed with care. We have adopted the method presented in Pavlidou et al. (2012), which takes into account the various limitations involved in dealing with real data. Table 6 reports the correlation coefficients r and the chances of obtaining a correlation coefficient at least as high as r from uncorrelated data having the same dynamic range in radio flux density, gamma-ray energy flux and luminosity distance as those observed.

From the analysis of the correlation coefficients, it is possible to see that the correlation becomes stronger as the radio frequency

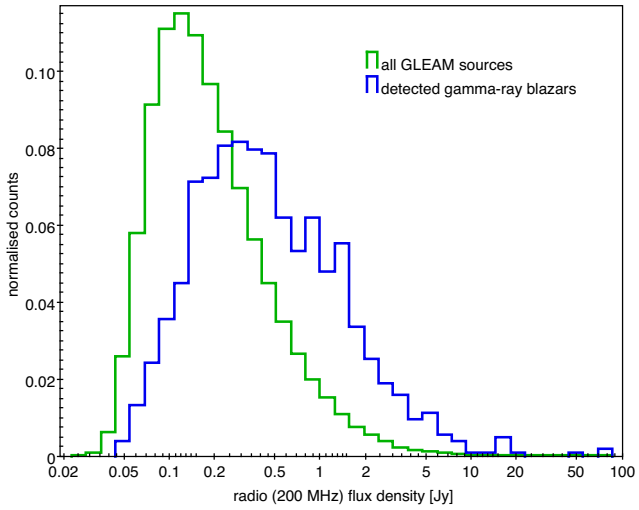

Figure 5. Low-frequency flux density distribution: blazars are brighter than the rest of the GLEAM sources.

increases. This behaviour is in accordance with the results reported in Ackermann et al. (2011a), Mahony et al. (2010), Ghirlanda et al. (2010, 2011) and G16, and is ascribed to the different amounts of relativistic Doppler boosting affecting regions with different spectral properties. In detail, the emission at low frequency (200 MHz) is largely produced in extended lobes, which are not beamed, while there is beaming at higher frequency (1 GHz) and in the gamma energy flux at $E > 100$ MeV.

It is worth noting that the correlation is more important for brighter radio sources, such as LSPs and FSRQs. Actually, most FSRQs are also LSPs. However, Fan & Wu (2018) find that the correlation is weaker for FSRQs than for BL Lacs, many of which are HSPs. Evidently, this must be becasue of the low depth survey (i.e. the TGSS) used by the authors, in which only the brightest BL Lacs are detectable. This bias influences the relative core dominance for these sources, showing BL Lacs as more core dominated than FSRQs.

4.5 Core and extended radio emission

The total flux density detected from a radio source can be separated into two spectrum components, following the relation

$$S_\nu = S_{\nu,\mathrm{lobe}} + S_{\nu,\mathrm{core}} = K_{\mathrm{lobe}}\,\nu^{\alpha_{\mathrm{lobe}}} + K_{\mathrm{core}}\,\nu^{\alpha_{\mathrm{core}}}, \quad (1)$$

where K_{lobe} and K_{core} are two coefficients that describe the lobe and the core fraction of the total flux density, respectively (G16).

To estimate the emission ratio between the steep spectrum lobe and the flat spectrum core, we made use of the definition of spectral index in the frequency range of GLEAM, $\alpha = \log(S_1/S_2)/\log(\nu_1/\nu_2)$, where $\nu_1 = 72$ MHz and $\nu_2 = 231$ MHz.

The previous relations allow us to express the ratio between K_{lobe} and K_{core} as

$$\frac{K_{\mathrm{lobe}}}{K_{\mathrm{core}}} = \frac{-10^{\alpha\log(\nu_1/\nu_2)} \times \nu_2^{\alpha_{\mathrm{core}}} + \nu_1^{\alpha_{\mathrm{core}}}}{10^{\alpha\log(\nu_1/\nu_2)} \times \nu_2^{\alpha_{\mathrm{lobe}}} - \nu_1^{\alpha_{\mathrm{lobe}}}}. \quad (2)$$

We estimate α_{lobe}, α_{core} and α based on the mean spectral index of the samples GLEAM ($\alpha_{\mathrm{lobe}} = -0.77$, which is the value for all sources that are, for the vast majority, not blazars), 4LAC–AT20G ($\alpha_{\mathrm{core}} = -0.05$) and 4LAC–GLEAM ($\alpha = -0.44$), respectively.

We estimated a ratio $K_{\mathrm{lobe}}/K_{\mathrm{core}} \sim 37$. G16 found that the same ratio was computed with data based on MWACS instead of GLEAM, for a value of ∼75. The big difference between these two results is a result of the limited depth, sensitivity and extension of the MWACS, compared with GLEAM. In particular, MWACS can only observe objects with a bright extended emission, overestimating the contribution of these sources, whereas our present result shows how the core contribution is more important.

The values of K_{lobe} and K_{core} by themselves have little intrinsic meaning, as they represent the extrapolation of the relative contribution to zero frequency. However, they are useful to estimate the ratio of the flux density of the core and the lobe emission at each frequency, as provided by equation (1). In particular, we determined that, at ∼158 MHz, the two spectrum components equally contribute to the total spectrum as $S_{\mathrm{lobe}}/S_{\mathrm{core}} \sim 1$. Fan & Wu (2018) found $S_{\mathrm{lobe}}/S_{\mathrm{core}} \sim 1$ at ∼150 MHz, which is in good agreement with our result.

Moreover, we determined the ratio $K_{\mathrm{lobe}}/K_{\mathrm{core}}$ for each object of the sample originated by cross-matching 4LAC–GLEAM with 4LAC–AT20G, by using the values of the spectral indices for the single source. Fig. 7 shows the distribution of $\log K_{\mathrm{lobe}}/K_{\mathrm{core}}$ for all sources in the sample. The distribution can be described with a Gaussian, with a central value that is in the bin between 26 and 38.

5 DISCUSSION AND CONCLUSIONS

Because of the improved sensitivity, bandwidth and sky coverage that GLEAM provides with respect to MWACS, we have been able to substantially characterize the radio spectrum of gamma-ray blazars in the very low radio frequency band ($\nu < 240$ MHz).

(i) We have provided more characterized results than the previous paper (G16) because of the better technical features of GLEAM compared with MWACS. In particular, we have detected more and much fainter sources, which were not detectable using MWACS because of its limited detection threshold and smaller sky area. We have also increased the number of objects as a result of using GLEAM and the 4LAC catalogue. In detail, the total number of gamma-ray blazars detected at low frequency has increased from 87 to 1274 (a factor of 14.6×) and the detection rate has increased from 35 to 70 per cent (a factor of 2×). FSRQs remain the class with the highest detection rate, reaching as high as 92 per cent. In other words, almost every gamma-ray FSRQ is detected at low frequency. However, BL Lacs and BCUs showed a larger fractional increase (from 22 to 58 per cent and from 18 to 66 per cent, respectively), mainly driven by the fact that BL Lacs tend to be fainter radio sources.

(ii) Despite the huge increase in sensitivity (GLEAM is 90 per cent complete at 170 mJy and 50 per cent complete at 55 mJy), several blazars that are moderately bright at GHz frequencies (well above the GLEAM completeness levels) remain undetected at $\nu < 240$ MHz. Such objects must have inverted spectra or be very variable sources. Another possibility could be that these objects do not have prominent plumes and lobes. In all these scenarios, this indicates that the extended emission contributes very little to their total emission at low frequency.

(iii) Blazars are well known for being characterized by flat spectra at high radio frequency, which is actually considered one of their defining features. Our work shows that at low radio frequency these sources continue to have flat spectra, both when considered as a unique population ($\alpha = -0.44 \pm 0.01$) and when they are divided into the different subclasses (when classified based on either their SEDs or their spectra). This result is shown in Fig. 4, where we can see that gamma-ray blazars have flatter spectra than the rest of the

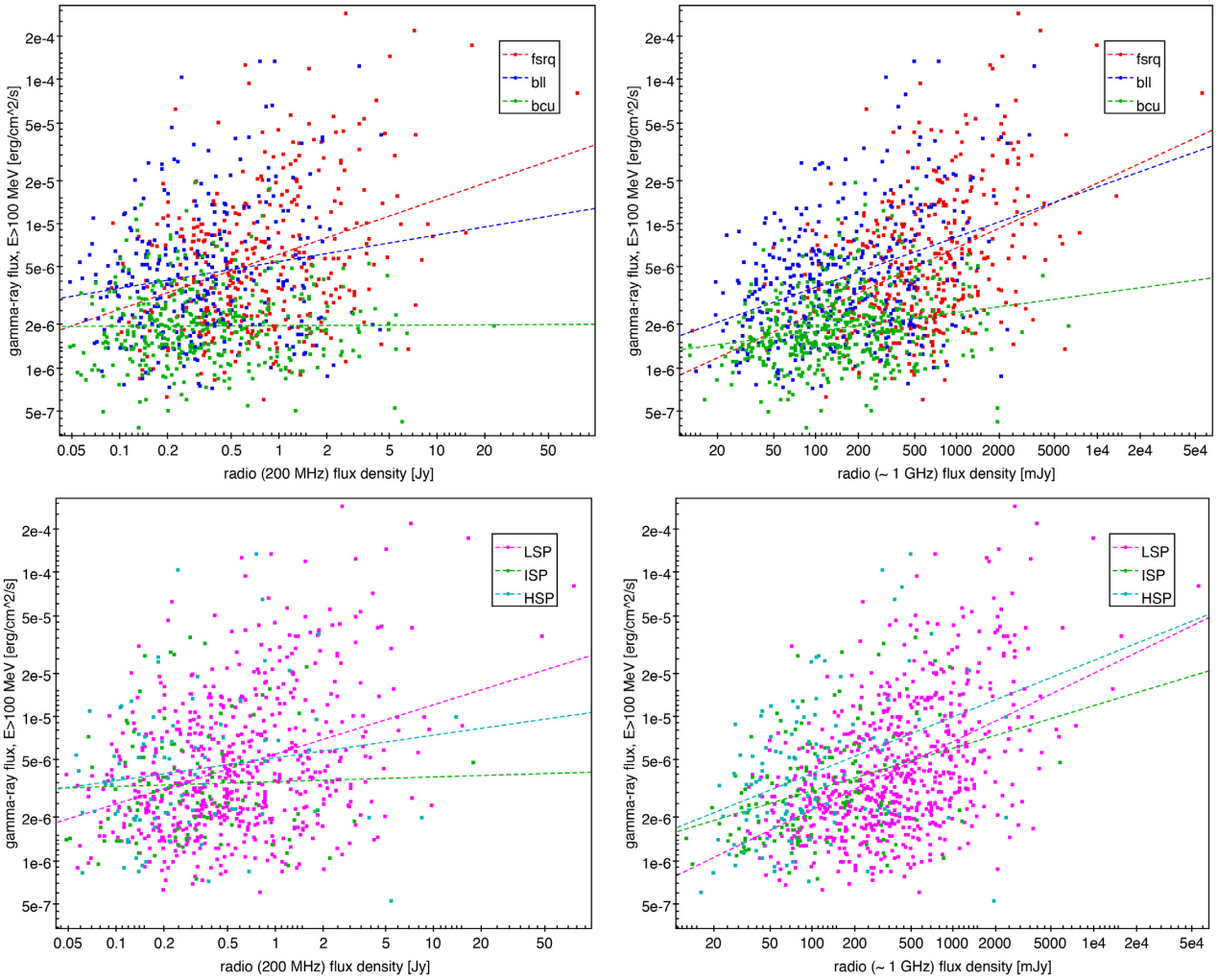

Figure 6. Gamma-radio correlations at 200 MHz (left) and at 1 GHz (right) for the GLEAM-detected blazars, classified based on their spectra (top panels) or on their SED peak (bottom panels). The radio flux densities at 200 MHz and at 1 GHz have been obtained from GLEAM and 4LAC, respectively.

Table 6. Coefficients of correlations r at 200 MHz and 1 GHz, with the statistically significant q-values, estimated using the method of Pavlidou et al. (2012).

Class	200 MHz		1 GHz	
	r	q-value	r	q-value
Total	0.27	$<10^{-6}$	0.41	$<10^{-6}$
FSRQ	0.24	0.0003	0.33	$<10^{-6}$
BCU	0.03	0.88	0.16	0.55
BLL	0.18	0.25	0.34	0.004
LSP	0.34	$<10^{-6}$	0.47	$<10^{-6}$
ISP	0.12	0.59	0.29	0.14
HSP	0.07	0.64	0.18	0.19

GLEAM sources in the ∼100 MHz regime. This result is not only in agreement with what was found by Massaro et al. (2013a) and Nori et al. (2014), but it actually extends those preliminary findings: to a much higher statistical significance (as reported in Table 3) and to an even lower frequency domain. Therefore, we can state that the core contribution to the total radio emission remains substantial, providing a useful diagnostic for classifying blazars in future sky surveys.

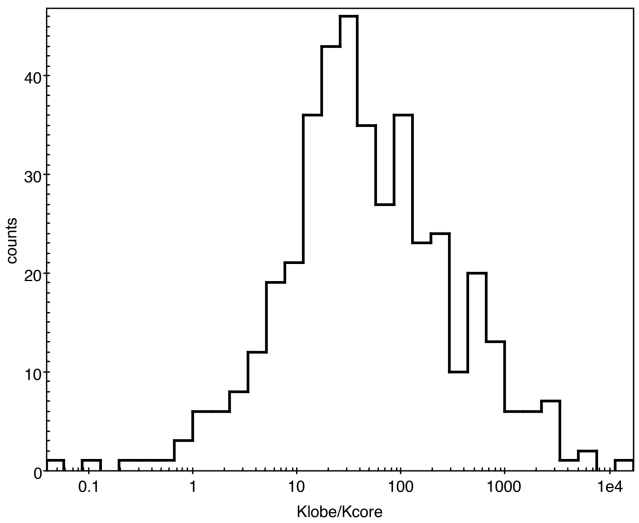

Figure 7. Distribution of the ratio $K_{\rm lobe}/K_{\rm core}$ for the 367 objects of the 4LAC–GLEAM versus 4LAC–AT20G cross-matching.

(iv) The fact that the core emission still contributes significantly to the total radio flux density in the GLEAM band is also supported by the presence of a significant correlation between the gamma-ray energy flux and the low radio frequency flux density. However, the presence of a much higher scatter in this correlation with respect to those found at higher frequencies (Ghirlanda et al. 2010, 2011; Mahony et al. 2010; Ackermann et al. 2011a) shows that the lobes are also very prominent at low frequency and that they are not significantly correlated with the core emission. In other words, the range of amplification due to the Doppler beaming of the gamma-ray emission is much wider than the intrinsic scatter of the correlation between core and lobe radio power in the rest frame.

(v) The availability of flux density and spectral indices (both intra- and inter-band) for a sizeable sample of sources, at low (<240 MHz, from GLEAM), intermediate (∼1 GHz, from 4LAC, in turn taken from NVSS or SUMSS) and high (20 GHz, from AT20G) frequency, allows us to estimate the relative contributions of the core and lobe radio emission in gamma-ray blazars. We compare the lobe and the core contribution of radio sources by estimating a mean 'zero-frequency' ratio $K_{\rm lobe}/K_{\rm core} \sim 37$, which indicates that the core and lobes have about the same power at 158 MHz. This ratio is lower than the value estimated in G16. This difference is due to the better technical features of GLEAM, which allowed the detection of sources with flatter spectra (and hence more core-dominated). We can thus predict that even deeper low-frequency surveys will further move the balance to less prominent radio lobes (although for FSRQs we already are near the 100 per cent detection rate, so we do not expect any dramatic change). Once calibrated with a sizeable sample of sources of different types, the low-frequency spectral index could become a quick indicator of core dominance and therefore a suitable proxy for the Doppler factor of gamma-ray blazars.

ACKNOWLEDGEMENTS

We thank the referee, F. Massaro, for comments and suggestions that helped to improve the paper. We thank V. Pavlidou for granting us permission to use the code for the computation of the significance of the correlation. We acknowledge financial support through grant PRIN-INAF ob. fun. 1.05.01.88.06. This research has made use of the SIMBAD data base, operated at CDS, Strasbourg, France. This research has also made use of NASA's Astrophysics Data System.

The authors of this work used the catalogues GLEAM and AT20G, which were realized thanks to the Murchison Radio-astronomy Observatory and the Australia Telescope Compact Array, over the administration of the CSIRO. The Australian Government provided the necessary financial support for the MWA and the ATCA.

REFERENCES

Abdo A. A. et al., 2009, ApJS, 183, 46
Abdo A. A. et al., 2010a, ApJS, 188, 405
Abdo A. A. et al., 2010b, ApJS, 188, 405
Abdo A. A. et al., 2010c, ApJ, 716, 30
Acero F. et al., 2015, ApJS, 218, 23
Ackermann M. et al., 2011a, ApJ, 741, 30
Ackermann M. et al., 2011b, ApJ, 743, 171
Ackermann M. et al., 2015, ApJ, 810, 14
Álvarez Crespo N. et al., 2016, Ap&SS, 361, 316
Blandford R. D., Rees M. J., 1978, in Wolfe A. M., ed., Pittsburgh Conference on BL Lac Objects. University of Pittsburgh Press, Pittsburgh, p. 328
Condon J. J., Cotton W. D., Greisen E. W., Yin Q. F., Perley R. A., Taylor G. B., Broderick J. J., 1998, AJ, 115, 1693
Fan X-L., Wu Q., 2018, ApJ, 869, 133
Fermi-LAT collaboration, 2019a, preprint (arXiv:1902.10045)
Fermi-LAT collaboration, 2019b, preprint (arXiv:1905.10771)
Ghirlanda G., Ghisellini G., Tavecchio F., Foschini L., 2010, MNRAS, 407, 791
Ghirlanda G., Ghisellini G., Tavecchio F., Foschini L., Bonnoli G., 2011, MNRAS, 413, 852
Giroletti M. et al., 2016, A&A, 588, A141 (G16)
Healey S. E., Romani R. W., Taylor G. B., Sadler E. M., Ricci R., Murphy T., Ulvestad J. S., Winn J. N., 2007, ApJS, 171, 61
Helfand D. J., White R. L., Becker R. H., 2015, ApJ, 801, 26
Hurley-Walker N. et al., 2014, PASA, 31, e045
Hurley-Walker N. et al., 2017, MNRAS, 464, 1146
Intema H. T., Jagannathan P., Mooley K. P., Frail D. A., 2017, A&A, 598, A78
Ivezić Ž. et al., 2002, AJ, 124, 2364
Kimball A. E., Ivezić Ž., 2008, AJ, 136, 684
Komatsu E. et al., 2009, ApJS, 180, 330
McConnell D., Sadler E. M., Murphy T., Ekers R. D., 2012, MNRAS, 422, 1527
Mahony E. K., Sadler E. M., Murphy T., Ekers R. D., Edwards P. G., Massardi M., 2010, ApJ, 718, 587
Marchesi S., Kaur A., Ajello M., 2018, AJ, 156, 212
Massaro F., D'Abrusco R., Giroletti M., Paggi A., Masetti N., Tosti G., Nori M., Funk S., 2013a, ApJS, 207, 4
Massaro F., Giroletti M., Paggi A., D'Abrusco R., Tosti G., Funk S., 2013b, ApJS, 208, 15
Massaro F., Giroletti M., D'Abrusco R., Masetti N., Paggi A., Cowperthwaite P. S., Tosti G., Funk S., 2014, ApJS, 213, 3
Massaro E., Maselli A., Leto C., Marchegiani P., Perri M., Giommi P., Piranomonte S., 2015, Ap&SS, 357, 75
Massaro F. et al., 2016, Ap&SS, 361, 337
Mauch T., Murphy T., Buttery H. J., Curran J., Hunstead R. W., Piestrzynski B., Robertson J. G., Sadler E. M., 2003, MNRAS, 342, 1117
Mooney S. et al., 2019, A&A, 622, A14
Murphy T. et al., 2010, MNRAS, 402, 2403
Nolan P. L. et al., 2012, ApJS, 199, 31
Nori M., Giroletti M., Massaro F., D'Abrusco R., Paggi A., Tosti G., Funk S., 2014, ApJS, 212, 3
Paiano S., Landoni M., Falomo R., Treves A., Scarpa R., 2017a, ApJ, 844, 120
Paiano S., Falomo R., Franceschini A., Treves A., Scarpa R., 2017b, ApJ, 851, 135
Pavlidou V. et al., 2012, ApJ, 751, 149
Peña-Herazo H. A. et al., 2017, Ap&SS, 362, 228
Stickel M., Padovani P., Urry C. M., Fried J. W., Kuehr H., 1991, ApJ, 374, 431
Taylor M. B., 2005, in Shopbell P., Britton M., Ebert R., eds, ASP Conf. Ser. Vol. 347, Astronomical Data Analysis Software and Systems XIV. Astron. Soc. Pac., San Francisco, p. 29
Tingay S. J. et al., 2013, PASA, 30, e007
Urry C. M., Padovani P., 1995, PASP, 107, 803

This paper has been typeset from a TEX/LATEX file prepared by the author.